

# RSC Applied Interfaces

Accepted Manuscript

This article can be cited before page numbers have been issued, to do this please use: A. Firdous, N. Abdillah, K. Hayashi, Y. Koda, M. Mesuda, K. Toko, S. Honda and T. Suemasu, *RSC Appl. Interfaces*, 2026, DOI: 10.1039/D6LF00069J.



This is an Accepted Manuscript, which has been through the Royal Society of Chemistry peer review process and has been accepted for publication.

Accepted Manuscripts are published online shortly after acceptance, before technical editing, formatting and proof reading. Using this free service, authors can make their results available to the community, in citable form, before we publish the edited article. We will replace this Accepted Manuscript with the edited and formatted Advance Article as soon as it is available.

You can find more information about Accepted Manuscripts in the [Information for Authors](#).

Please note that technical editing may introduce minor changes to the text and/or graphics, which may alter content. The journal's standard [Terms & Conditions](#) and the [Ethical guidelines](#) still apply. In no event shall the Royal Society of Chemistry be held responsible for any errors or omissions in this Accepted Manuscript or any consequences arising from the use of any information it contains.

## Exploring the potential of BaS as a hole transport layer for BaSi<sub>2</sub> solar cells: thin-film growth and oxygen-related defect characterization using first-principles calculation

Ammara Firdous,<sup>1</sup> Nurfauzi Abdillah,<sup>1</sup> Koki Hayashi,<sup>1</sup> Yoichiro Koda,<sup>2</sup> Masami Mesuda,<sup>2</sup> Kaoru Toko,<sup>3</sup> Syuta Honda<sup>4</sup>, Takashi Suemasu<sup>3</sup>

<sup>1</sup>Graduate School of Science and Technology, University of Tsukuba, Ibaraki 305-8573, Japan<sup>0</sup>

<sup>2</sup>Advanced Materials Research Laboratory, Tosoh Corporation, Ayase, Kanagawa 252-1123, Japan

<sup>3</sup>Department of Applied Physics, Institute of Pure and Applied Sciences, University of Tsukuba, Ibaraki 305-8573, Japan

<sup>4</sup>Department of Pure and Applied Physics, Kansai University, Suita, Osaka 564-8680, Japan

Barium disilicide (BaSi<sub>2</sub>) is a promising non-toxic and abundant material for thin-film solar cells due to its large optical absorption coefficient and a suitable bandgap of 1.3 eV. However, due to its small electron affinity ( $EA = 3.2$  eV), oxide-based hole transport layer (HTL) materials used in crystalline silicon solar cells cause a large valence band offset at the HTL/BaSi<sub>2</sub> interface, hindering hole transport. In this study, barium sulfide (BaS) is proposed as an effective HTL for BaSi<sub>2</sub>-based solar cells. This is the first combined experimental and first-principles study of sputtered BaS thin films focusing on their electronic structure, ionization potential, and oxygen-related defect properties for HTL applications. Spectroscopic ellipsometry evaluation of the BaS absorption edge yielded an indirect bandgap of approximately 3.6 eV. Ultraviolet photoelectron spectroscopy results indicate an ionization potential ( $IP$ ) of approximately 4.3 eV. These results indicate that BaS is a good HTL candidate for BaSi<sub>2</sub> solar cell applications; however, the measured  $IP$  value is comparable or slightly smaller than those reported previously. To better understand the origin of point defects in BaS, first-principles defect calculations were conducted under various Ba, S, and oxygen (O)-chemical potential conditions. Oxygen was taken into account because it is an element that is difficult to avoid during thin-film growth and other processes, and because BaSi<sub>2</sub> films formed by sputtering—which form heterojunctions with BaS—contain more than  $10^{20}$  cm<sup>-3</sup> of oxygen. The calculation results indicate that among various point defects interstitial atoms of



Ba and O ( $O_i$ ), and O substituted for S antisites ( $O_S$ ) readily form;  $O_S$  does not alter the electronic properties of BaS, while  $O_i$  can be regarded as shallow acceptor defects.

**KEYWORDS:** BaSi<sub>2</sub>, BaS, thin film, sputtering, first-principles calculation, point defects,

\*Email: [suemasu.takashi.gu@u.tsukuba.ac.jp](mailto:suemasu.takashi.gu@u.tsukuba.ac.jp)



## Introduction

Toward realizing a sustainable society, photovoltaic technology is becoming increasingly important. Currently, crystalline silicon solar cells account for over 95% of the global market, and conversion efficiency has exceeded 27% at the research level.<sup>1</sup> However, due to its low light absorption coefficient and relatively small bandgap ( $E_g = 1.1$  eV), the development of wafer-based device structures is essential. This limits mechanical flexibility and restricts installation to flat surfaces. To overcome these limitations, numerous developments have been pursued in thin-film solar cell materials such as GaAs, CdTe, and Cu(In,Ga)(Se,S)<sub>2</sub>, as well as halide perovskites.<sup>1</sup> While these materials offer high conversion efficiency, barriers exist to their sustainable and widespread adoption. This is because they rely on limited or harmful elements such as As, Cd, Te, and Pd. We have focused particularly on semiconducting barium disilicide (BaSi<sub>2</sub>). BaSi<sub>2</sub> is composed of non-toxic and abundant elements. This material is an indirect semiconductor with a band gap of around 1.3 eV,<sup>2,3</sup> which is suitable for single-junction solar cells. In addition, since it possesses a direct transition edge only 0.1 eV above the band gap,<sup>3,4</sup> both a high optical absorption coefficient with an abrupt onset around the band gap due to the localized Ba-d states at the conduction band minimum<sup>3</sup> and excellent minority carrier properties such as a large minority-carrier diffusion length ( $\sim 10$   $\mu\text{m}$ ) are available in BaSi<sub>2</sub>.<sup>5-8</sup> Solar cell materials with these characteristics are rare. For these reasons, BaSi<sub>2</sub> has garnered significant attention as a thin-film absorber layer.<sup>9-12</sup> So far extensive efforts have been devoted to enhancing device performance by exploring several layered structures, including heterojunctions such as BaSi<sub>2</sub>/Si,<sup>13-15</sup> ZnO/BaSi<sub>2</sub>,<sup>16</sup> SnS/BaSi<sub>2</sub>,<sup>17</sup> and homojunctions,<sup>18,19</sup> and various device structures have been proposed.<sup>20-25</sup> Among them, the p-BaSi<sub>2</sub>/n-type crystalline Si heterojunction diode formed by vacuum evaporation has achieved the highest conversion efficiency of 10.62% under AM1.5 irradiation to date.<sup>14</sup> As BaSi<sub>2</sub> possesses a high optical absorption coefficient, when used as a surface layer, significant parasitic absorption occurs due to defects in the BaSi<sub>2</sub>.<sup>16</sup> To solve this problem, solar cell structures where a BaSi<sub>2</sub> absorber layer is sandwiched between an electron transport layer (ETL) and a hole transport layer (HTL) with a wide  $E_g$  have been proposed.<sup>26-30</sup> The electron affinity ( $EA$ ) of BaSi<sub>2</sub> is relatively low at 3.2 eV,<sup>31</sup> allowing a wide range of materials to be considered as ETL candidates. Furthermore, its ionization potential ( $IP$ ) is relatively small at 4.5 eV,<sup>32</sup> making the selection of an appropriate HTL more challenging. HTL materials are classified into two types: type-I and type-II, differing significantly based on the presence or



absence of a valence band offset at the HTL/BaSi<sub>2</sub> interface. At the type-I HTL/BaSi<sub>2</sub> interface, the valence band offset is small or absent, allowing photogenerated holes in BaSi<sub>2</sub> to drift directly across the interface.<sup>33,34</sup> Conversely, at the type II-HTL/BaSi<sub>2</sub> interface, photogenerated holes are transported via defects or interband transitions.<sup>35</sup> Figure 1 shows the band alignment of BaSi<sub>2</sub> with HTL candidates such as NiO,<sup>36,37</sup> Cu<sub>2</sub>O,<sup>38</sup> MoO<sub>3</sub>,<sup>39,40</sup> WO<sub>3</sub>,<sup>41-43</sup> and V<sub>2</sub>O<sub>5</sub>.<sup>44</sup> Among them, NiO and Cu<sub>2</sub>O are type-I HTL materials for BaSi<sub>2</sub> solar cells, while V<sub>2</sub>O<sub>5</sub>, WO<sub>3</sub>, and MoO<sub>3</sub> are type-II HTL materials. For example, MoO<sub>3</sub>, which has been used as a type-II HTL material in crystalline Si solar cells, has achieved a high conversion efficiency of 23.8%.<sup>45</sup> However, since BaSi<sub>2</sub> readily reacts with oxygen, it is not easy to use these oxide-based HTL materials.<sup>46</sup> Under these circumstances, BaS is investigated in our work as a potential type-I HTL material for BaSi<sub>2</sub> solar cell applications.

BaS is an alkaline-earth chalcogenide (IIa-VIb) semiconductor with space group of  $Fm\bar{3}m$  as shown in Figure 2, and is chemically stable and inert to BaSi<sub>2</sub>.<sup>27</sup> It has the same crystal structure as NaCl and the lattice constant is approximately 0.64 nm.<sup>47,48</sup> BaS bulk crystals have been mainly formed by reducing BaCO<sub>3</sub><sup>46,47</sup> or BaSO<sub>4</sub>.<sup>48,49</sup> BaS is an indirect bandgap semiconductor with an  $E_g$  of approximately 3.8 eV as determined by the optical properties of bulk crystals<sup>49,50</sup> and first-principles calculation using the Heyd–Scuseria–Ernzerhof (HSE06) hybrid functional explained the reported  $E_g$  well when a default mixing parameter was set to 45%.<sup>53</sup> The  $EA$  of BaS was measured to be 0.84 eV based on the temperature dependences of the thermionic emission and electrical conductivity.<sup>51</sup> Furthermore, its  $IP$  was estimated to be 4.9 eV from the photoemission spectrum.<sup>49</sup> These characteristics make it a favorable candidate for a type-I HTL for BaSi<sub>2</sub> solar cell applications. However, these properties were measured in BaS bulk crystals, not in BaS thin films intended for devices. This is because, although the atomic layer growth method exists for forming BaS films,<sup>54</sup> no other method capable of large-area deposition has been reported. Among various thin-film growth methods, we selected radio-frequency (RF) sputtering for the deposition of BaS thin films. This selection was made because BaSi<sub>2</sub> films formed by RF sputtering recently achieved a photoresponsivity of 15 A/W,<sup>55</sup> the highest value ever reported. Therefore, it enables the in-situ formation of BaS films after BaSi<sub>2</sub> deposition.

Previous experimental studies have shown that BaS is highly sensitive to deviations from stoichiometry.<sup>52</sup> In S-rich environments, while the host crystal structure remains unchanged, S-related defects primarily affecting recombination behavior emerge. Collectively, these studies



indicate that BaS is a structurally robust yet defect-prone material, offering scope for systematic exploration of the physical properties of these defects. Recent comprehensive defect calculations indicate that the electronic properties of BaS are primarily influenced by intrinsic point defects.<sup>53</sup> Under Ba-rich conditions, S vacancies dominate and act as shallow donors, whereas under S-rich conditions, significant self-compensation between donor and acceptor defects inhibits effective p-type conductivity. It was suggested that interstitial atoms (Li, Na, K, and Rb) yield high n-type conductivity and their substitutions at Ba sites result in mild p-type behavior. However, these computational simulations have not taken oxygen (O) into account. Measurements using secondary ion mass spectrometry have shown that BaSi<sub>2</sub> thin films formed by co-sputtering of BaSi<sub>2</sub> and Ba targets contain more than 10<sup>20</sup> cm<sup>-3</sup> of oxygen.<sup>56</sup> Therefore, if BaS forms on a BaSi<sub>2</sub> thin film, it is quite possible that oxygen will diffuse into the BaS. Furthermore, since oxygen is an unavoidable impurity during thin-film fabrication and subsequent processes, it is important to take the effects of oxygen into account. This study addresses this existing gap by integrating sputtered BaS thin film fabrication with first-principles defect calculations that accurately account for O under varying Ba, S, and O chemical potential conditions. This extends the previously studied stoichiometric framework and provides a realistic evaluation of BaS in sputter-deposited thin films for BaSi<sub>2</sub>-based solar cell applications.

## Experimental details

BaS thin films were deposited on Czochralski n<sup>+</sup>-type Si (111) substrates with a resistivity  $\rho < 0.01 \text{ } \Omega \text{ cm}$  using RF magnetron sputtering (ULVAC MB00- 1040) using a 1-inch diameter stoichiometric BaS target provided by Furuuchi Chemical. Inc. The substrate temperature ( $T_S$ ) during film deposition was set in the range 300–600 °C. The Ar gas pressure was set to 0.5 Pa. The deposited films were covered with a 3 nm thick amorphous Si (a-Si) capping layer to prevent oxidation.<sup>57</sup> The grown layer thickness was measured by a surface profiler (KLA Apha-Step D-500). Table 1 summarizes sample preparation details.

Table 1. Growth conditions of BaS thin-film samples: substrate temperature during deposition ( $T_S$ ), BaS deposition thickness ( $d_{\text{BaS}}$ ), and a-Si capping thickness ( $d_{\text{a-Si}}$ ).

Sample	$T_S$ (°C)	$d_{\text{BaS}}$ (nm)	$d_{\text{a-Si}}$ (nm)
--------	------------	-----------------------	------------------------



A	300	20	3
B	400	20	3
C	475	20	3
D	500	20	3
E	525	20	3
F	600	20	3
G	500	70	3

The crystalline quality of grown films was evaluated by grazing-incidence x-ray diffraction (GI-XRD: Rigaku SmartLab) measurements with a Cu K $\alpha$  radiation source. The incident angle of x-rays was set to 0.4° from the sample plane to enhance the penetration depth in the BaS films x-rays travel. Using ultraviolet photoelectron spectroscopy (UPS: PHI Versa Probe, ULVAC-PHI) with He-I lines (21.22 eV) and an applied bias voltage of -10 V, the *IP* of BaS films was measured. A charge neutralizer was utilized to reduce the charging effects caused by electron emission during the measurement. Spectroscopic ellipsometry (HORIBA UVISSEL PLUS) was used to assess the optical absorption edge of BaS films.

### Computational details

All density functional theory (DFT) calculations were carried out using the projector-augmented wave (PAW) method within the Vienna ab initio Simulation Package (VASP).<sup>58-60</sup> PAW pseudopotentials for Ba( $5s^2 5p^6 5d^{0.01} 6s^{1.99}$ ), S( $3s^2 3p^4$ ), and O( $2s^2 2p^4$ ) were used in all calculations. The exchange-correlation interactions have been investigated via the generalized gradient approximation with the Perdew-Burke-Ernzerhof (GGA-PBE) functional.<sup>61</sup> The electronic self-consistent-field calculations and geometry optimizations both converged at 10<sup>-5</sup> eV. Geometry optimizations were carried out via the conjugate-gradient algorithm along with a Monkhorst-Pack *k*-point sampling technique.<sup>62</sup> The BaS crystal was modeled with a cubic unit cell that included 8 atoms as shown in Figure 2. The lattice constants were set as  $a = b = c = 0.64513$  nm and the lattice angles were set to  $\alpha = \beta = \gamma = 90^\circ$ . The Brillouin zone was sampled using a  $5 \times 5 \times 5$  *k*-point mesh. When optimizing the geometry, the cell's form and volume stayed the same, and only the positions of the atoms inside the cell were permitted to relax to their lowest-



energy states. The structural and electrical characteristics of BaS are reliably described by this computational configuration, which also offers a consistent foundation for further electronic structure and defect calculations.<sup>63</sup> A cubic BaS supercell using a 64-atom ( $2 \times 2 \times 2$ ) configuration was utilized for charged defect calculations, and defect energetics<sup>64</sup> were assessed using the supercell method under periodic boundary conditions. For defect  $D$  in the charge state  $q$ , the formation energy  $\Delta H(D^q)$  is expressed as,<sup>65</sup>

$$\Delta H(D^q) = E_{tot}(D^q) - E_{tot}(bulk) - \sum_i \Delta n_i \mu_i + q(E_V + E_F + \Delta V) + E_{corr}. \quad (1)$$

Here,  $E_{tot}(D^q)$  is the total energy of BaS containing defect  $D$ , and  $E_{tot}(bulk)$  is the reference total energy of the defect-free BaS.  $\Delta n_i$  denotes the number of species  $i$  ( $i = \text{Ba, S, or O}$ ) added ( $\Delta n_i > 0$ ) to or removed ( $\Delta n_i < 0$ ) from the supercell.  $\mu_i$  is the chemical potential of species  $i$  referred to the standard elemental state, *i.e.*,  $\mu_i = \mu_i^0 + \Delta\mu_i$ , where the reference potentials  $\mu_i^0$  are those of an elemental solid or gas.  $E_V$  is the valence band maximum (VBM) of neutral bulk BaS, and  $E_F$  is the Fermi energy.  $\Delta V$  is a vertical shift correction applied to all charged defects. In this study, this term was set up to zero.<sup>66</sup> This selection is justified by the cubic symmetry of BaS.  $E_{corr}$  provides exclusive imaginary electrostatic interactions between regularly repeating charged defects and their compensatory background charge. In this study, solely the image-charge correction was executed, expressed as<sup>67</sup>

$$E_{corr} = [1 + f] \frac{q_i^2}{2\epsilon L}. \quad (2)$$

Here,  $q_i$  represents the charge state of defect  $i$ ,  $\epsilon$  represents the static dielectric constant of BaS,  $L$  signifies the effective supercell dimension, and  $f$  is the geometry-dependent quantity that accounts for higher-order electrostatic contributions. No supplementary correction term  $C(D^q)$  was introduced. This approach complies to the electrostatics-based correction framework, demonstrating that for cubic crystals showing isotropic dielectric screening, the image-charge correction completely accounts for the main finite-size effects, making the explicit Coulomb divergence correction term  $C(D^q)$  inapplicable. Furthermore, electronic structural calculations were conducted to evaluate the electronic properties of BaS. An analysis of the total and projected density of states (DOS) was also conducted. All DOS charts were produced utilizing the PyProcar package, which provides extensive post-processing and visualization of VASP output data, while the corresponding atomic structures and defect configurations have been shown using the Visualization for Electronic and Structural Analysis (VESTA) software.<sup>68</sup>



## Results and discussion

### Thin film growth and film properties

Figure 3 shows the correlation between the input RF power applied to the BaS target and the BaS deposition rate obtained in this work. It was confirmed that the deposition rate consistently increased with increasing the input RF power. In the experiment, this calibration result was used to select an input power of 50 W. At this power, the deposition rate was approximately  $0.15 \text{ nm min}^{-1}$  at an Ar gas pressure of 0.5 Pa.

Figure 4 shows the GI-XRD patterns of samples A–F formed at substrate temperatures between 300 and 600 °C. The calculation results for BaSi<sub>2</sub> and BaS are also presented. These were calculated using the commercial software CaRine Crystallography, based on the lattice constants and space groups of these two materials. BaSi<sub>2</sub> has an orthorhombic crystal with the space group *Pnma* (lattice constants:  $a = 0.891 \text{ nm}$ ,  $b = 0.672 \text{ nm}$ , and  $c = 1.153 \text{ nm}$ ).<sup>69</sup> For sample A ( $T_s = 300 \text{ °C}$ ), no evident diffraction peaks were observed corresponding to BaSi<sub>2</sub> or BaS, signifying that the films were mostly amorphous. Upon elevating the  $T_s$  to 400 °C (sample B), a broad peak emerged at  $2\theta \sim 25^\circ$ , indicating the initiation of short-range ordering. When  $T_s$  was increased to 475 °C (sample C), 500 °C (sample D), and 525 °C (sample E), distinct diffraction peaks such as  $2\theta \approx 23.9^\circ$ ,  $27.6^\circ$ , and  $39.5^\circ$  appeared, which correspond to the 111, 200, 220 diffractions of BaS, respectively, aligning with the calculated BaS reference peak positions. Moreover, the diffraction peaks increased in intensity and sharpness as  $T_s$  was increased to 500 °C, signifying enhanced crystallinity and the development of a polycrystalline BaS phase. For sample F, deposited at 525 °C (sample E), however, a distinct peak at  $2\theta \approx 25.0^\circ$  (red triangle) appeared in addition to those of BaS. This corresponds to the 334 diffract of BaSi<sub>2</sub>. When  $T_s$  was further increased to  $T_s = 600 \text{ °C}$  (sample F), the BaS diffraction peaks disappeared, indicating potential degradation or re-amorphization of the film, possibly due to re-evaporation of S at elevated temperatures. In BaS sputtering deposition, as the substrate temperature rises, S—which has a higher vapor pressure than Ba—is likely to re-evaporate, leading to crystal degradation. A similar phenomenon has been observed in ZnS sputtering deposition, where Zn deficiencies become apparent as the substrate temperature increases.<sup>70</sup> The lattice constants of the cubic BaS was estimated from the three peaks corresponding to 111, 200, and 220 diffractions using Bragg's law. They are 0.653 nm, 0.644 nm, and 0.652 nm for samples formed at  $T_s = 475 \text{ °C}$  (sample C), 500 °C (sample D), and 525 °C



(sample E), respectively, indicating a slight  $T_S$  dependent variation. The XRD results indicate that a substrate temperature around 500 °C is optimal for the fabrication of polycrystalline BaS thin films. These deposition temperatures are significantly lower than the higher processing temperatures (800–1300 °C) required for crystallization of BaS in reduction reactions.<sup>50,52</sup> These results conclude that polycrystalline BaS thin films were successfully grown on Si (111) substrates using the conventional RF sputtering method.

Spectroscopic ellipsometry measurement was performed on a 70 nm thick BaS film in sample G, deposited at  $T_S = 500$  °C, to determine the optical absorption edge of BaS. The refractive index ( $n$ ) and extinction coefficient ( $\kappa$ ) were determined by analyzing the change in the polarization state of light upon reflection using an optical model based on dispersion equations as shown in Figure 5(a). The Tauc-Lorentz dispersion model was adopted for the a-Si and BaS layers.<sup>71-73</sup> From the extinction coefficient  $\kappa$ , the optical absorption coefficient  $\alpha$  was calculated using the formula  $\alpha = 4\pi\kappa\lambda^{-1}$ . Here,  $\lambda$  is the wavelength of the incident light. Figure 5(b) shows the  $(\alpha\hbar\nu)^{1/2}$  versus photon energy  $\hbar\nu$  plot. The indirect absorption edge was determined to be approximately 3.6 eV from the intersection of the extrapolated linear fit with the energy axis. This value is slightly smaller than those of BaS bulk crystals.<sup>49,50</sup> The observed reduction can be attributed to differences in synthesis methodology, microstructural disorder, and defect incorporation inherent to sputter-deposited thin films.

Figure 6 shows the UPS spectrum of a 20 nm-thick BaS thin film, deposited at  $T_S = 500$  °C, in sample D, after the a-Si capping layer was mildly etched in situ by Ar ions without air exposure. The  $IP$  of the BaS film was calculated using Eq. (3) by subtracting the spectral width of the UPS spectrum from the incident photon energy (21.22 eV).

$$IP = h\nu - (E_{k,\min} - E_V). \quad (3)$$

For semiconductors like BaS, at the position of  $E_{k,\min}$  in Figure 6, electrons with the lowest energy that overcomes the work function barrier are detected, while at the  $E_V$  position, electrons near the VBM are detected. They are 8.2 eV and  $-8.7 \pm 0.3$  eV, respectively. The ionization potential ( $IP$ ) for sample D, which is the energy separation between  $E_V$  and vacuum level, is therefore calculated to be  $IP = 4.3 \pm 0.3$  eV. This value is close to that of BaSi<sub>2</sub> ( $IP = 4.5$  eV),<sup>31</sup> indicating favorable valence-band alignment for hole transport across the BaS/BaSi<sub>2</sub> interface as shown in Fig. 7.

### First-principles calculation



### *Electronic properties*

Figure 8 shows the band structure of BaS calculated using the HSE functional. As reported previously, BaS is an indirect bandgap semiconductor, with the VBM located at the  $\Gamma$  point and the conduction-band minimum (CBM) at the X point.<sup>53,74</sup> The effective masses for electrons and holes are also provided in Figure 8. It is noted that they may be greater than the free electron mass depending on the carrier transport direction. The band gap is approximately 3.0 eV, which is nearly equivalent to those calculated using HSE,<sup>74,75</sup> but is underestimated compared to those reported by experiment.<sup>49,50</sup> The calculated value is closer to the experimental value compared to those calculated using GGA.<sup>76-79</sup> Y. Chen *et al.* explained that the mixing default parameter must be modified to obtain values closer to the experimental band gap.<sup>53</sup>

Figure 9(a) and 9(b) shows the calculated projected DOS for BaS using GGA and HSE functional, respectively. In both cases, the DOS clearly shows that states adjacent to the valence band edge are primarily attributed to S p states, while the conduction band edge is strongly influenced by Ba d states. The effective density of states estimated from the calculated DOS and the Fermi–Dirac distribution function at 300 K was approximately  $1.8 \times 10^{19} \text{ cm}^{-3}$  for electrons and  $7.5 \times 10^{19} \text{ cm}^{-3}$  for holes. The bandgap calculated with the HSE functional ( $\sim 3.0$  eV) in Figure 9(a) agrees better with the experimentally determined optical bandgap ( $\sim 3.6$  eV) presented in Figure 5(b) than that with the GGA ( $\sim 2.2$  eV) in Figure 9(b). However, since calculations using the HSE functional require enormous computational time, the GGA was adopted for the formation energy calculations of point defects in BaS discussed next. Similar calculations have also been performed in BaSi<sub>2</sub>.<sup>74</sup>

### *Point defects under O-rich conditions*

Figure 10 shows the relaxed atomic structures of interstitial defects in the BaS supercell: barium interstitials (Ba<sub>i</sub>) in Figure 10(a), sulfur interstitials (S<sub>i</sub>) in Figure 10(b), and oxygen interstitials (O<sub>i</sub>) in Figure 10(c), introduced at the interstitial site with fractional coordinates (0.125, 0.125, 0.125) and fully relaxed the local geometry. Arrows indicate the interstitial sites. Green, yellow, and red spheres represent Ba, S, and O, respectively.

Figure 11(a)–11(d) illustrates the calculated formation energies of intrinsic point defects in BaS under O-rich conditions as a function of the Fermi energy from the VBM, 0 eV, to the CBM,  $\sim 2.2$  eV across the four distinct conditions: Ba-rich/S-rich/O-rich, Ba-poor/S-poor/O-rich, Ba-



rich/S-poor/O-rich, and Ba-poor/S-rich/O-rich, respectively. The evaluated intrinsic defects include barium vacancies ( $V_{Ba}$ ), sulfur vacancies ( $V_S$ ), barium substituted for sulfur antisites ( $Ba_S$ ), sulfur substituted for barium antisites ( $S_{Ba}$ ),  $Ba_i$ , and  $S_i$ . Regarding oxygen-related defects, oxygen substituted for barium antisites ( $O_{Ba}$ ), oxygen substituted for sulfur antisites ( $O_S$ ), and  $O_i$  are considered. The slope of each line indicates the charge state  $q$ , and a kink on each line means the transition level ( $q/q'$ ) at which the predominant charge state is changed from  $q$  to  $q' = q + 1$  or  $q - 1$ . The defects that give the lower formation energy is considered to be thermodynamically stable, i.e., higher likelihood of formation. The lower the Fermi energy, the lower the electron density; the higher the Fermi energy, the higher the electron density. As shown in Figures 11(a) – 11(d), we can intuitively conclude that most of the point defect's formation energy alters dynamically according to the conditions of the system that is, the Fermi energy and the chemical potential of each element in the system (e.g. Ba-rich, S-rich, and O-rich). These variables are important to fully assess how the material behaves with respect to its fabrication conditions. The formation energy of each point defect is denoted with uniquely colored lines in the plot. One defect has a straight flat line throughout the Fermi energy range (i.e.  $O_S$ ) while the others show change in gradients. These different gradients show different charge state of the defects; positive gradient lines denote positively charged defects while the negative gradient lines denote negatively charged defects. The flat lines mean the defects are neutrally charged. The circular dots in between the change of gradient are what are generally termed as transition levels. For instance, the transition level between +1 charged state and neutrally charged state can be written as +1/0, which can be seen as the defect initially in a positively charged state (needing one electron) to a neutrally charged state by getting an electron from the system. In other words, it can also be interpreted as the transition level where a neutrally charged defect donates an electron to the system (i.e. acting as a donor). For 0/-1 transition, it can be interpreted as an acceptor. Other than that, charge transition levels (CTLs) closer to the CBM or VBM means it is a shallow donor or acceptor while the CTLs far from the CBM and VBM can be termed as deep donors or acceptors. Based on the above, we focus on the lowest formation energy point defects in every condition.

Under Ba-rich/S-rich/O-rich environments in Figure 11(a),  $Ba_i$ ,  $O_i$ , and  $O_S$  have the lower formation energy across the band gap. Among them,  $Ba_i$  has positively charged defect (+2) with no CTL in the band gap. Therefore,  $Ba_i$  does not contribute to the generation of carriers. On the other hand,  $O_i$  has negatively charged defects with 0/-1 and -1/-2 CTLs across the bandgap,



meaning that  $O_i$  may act as a shallow acceptor, since  $0/-1$  CTL is near the VBM.  $O_S$  has no kink within the band gap, meaning neutral charged defects. In Figure 11(b), under Ba-poor/S-poor/O-rich environments,  $Ba_i$ ,  $O_i$ , and  $O_S$  also have the lower formation energy across the band gap.  $O_S$  is much stabler among them because of the S-poor condition, allowing O atoms to occupy isoelectric S sites easier, forming  $O_S$ . In Figure 11(c), under Ba-rich/S-poor/O-rich environments,  $S_i$  has the  $+1/0$  CTL way below the CBM (nearer to VBM) and hence it is considered a deep donor defect. Such a deep donor defect is likely to behave recombination centers. Under Ba-poor/S-poor/O-rich environments, in Figure 11(d), the situation is almost the same as those in Figures 11(a) and 11(b).

#### *Point defects under O-poor conditions*

Figure 12(a)–12(d) illustrates the calculated formation energies of intrinsic point defects in BaS under O-poor conditions as a function of the Fermi energy from the VBM to CBM across four distinct conditions: Ba-rich/S-poor/O-poor, Ba-poor/S-poor/O-poor, Ba-rich/S-poor/O-rich, and Ba-poor/S-rich/O-poor. Interestingly, under O-poor conditions, the formation energy of  $O_S$  increases drastically, rendering it out of the thermodynamically stable point defects in Figure 12(d). Specifically, in Figures 12(a) and 12(c),  $O_i$  becomes the most stable defect across the entire bandgap. In  $BaSi_2$ , it is known that small atoms such as B, C, N, and O readily occupy interstitial sites.<sup>80</sup> Therefore, it is thought that the small size of O also contributes to this behavior in BaS. As discussed in Figure 11,  $O_i$  functions as an excellent shallow acceptor, inducing p-type conductivity in the material. This p-type conductivity aligns with the objective of utilizing BaS as HTL. Oxygen, being highly electronegative, is easy to form anions. It is therefore thought to release holes to compensate for the charge. Based on the formation energy diagrams in Figures 11 and 12, the following key insights were gained toward forming BaS films that function as HTL. O doping to form  $O_i$  can be an effective method for generating p-type BaS. However, it should be noted that  $O_S$ , which has a similarly low formation energy, is also formed. The  $O_S$  defect, when present at a concentration of about one per 64 atoms, is not an electrically active defect as demonstrated in this work. However, an increase in its concentration could potentially affect the properties of BaS.

## Conclusions

We demonstrated the formation of polycrystalline BaS thin films on Si (111) substrates via RF



sputtering using a BaS target. GI-XRD analyses indicated that BaS films deposited at substrate temperatures of 500 and 525 °C exhibit a well-defined rock-salt crystal structure. Optical absorption analysis further confirmed that sputter-deposited BaS thin films possess an indirect bandgap of approximately 3.6 eV and an ionization potential of approximately 4.3 eV, close to that of BaSi<sub>2</sub>. The experimentally verified band alignment demonstrated that BaS forms an energetically favorable interface with BaSi<sub>2</sub>, enabling efficient hole transport across the BaS(HTL)/BaSi<sub>2</sub>(light absorbing layer) interface. Furthermore, analysis of point defects via DFT supercell calculations revealed that interstitial defects such as Ba<sub>i</sub>, S<sub>i</sub>, and O<sub>i</sub>, as well as O<sub>s</sub>, readily form. Particularly under O-poor conditions, O<sub>i</sub> is most likely to occur, creating shallow acceptor levels. This indicates that moderate O doping renders p-type BaS, making it suitable as HTL in BaSi<sub>2</sub> solar cells. The findings in this work pave the way for the formation of BaS/BaSi<sub>2</sub> heterojunctions via sputtering.

### Author contributions

A. Firdous: writing – original draft, investigation, visualization, and formal analysis. N. Abdillah: investigation, and review, and editing. K. Hayashi: investigation, visualization, and formal analysis. Y. Koda: review, and editing. M. Mesuda: review, and editing. K. Toko: supervision, review, and editing. S. Honda: investigation, review, and editing. T. Suemasu: conceptualization, supervision, funding acquisition, review, and editing.

### Conflict of interest

There is no conflict of interest to declare.

### Acknowledgements

This work was financially supported in part by JSPS KAKENHI (Grant Nos. JP21H04548 and JP24KK0083). A part of this work was supported by “Advanced Research Infrastructure for Materials and Nanotechnology in Japan (ARIM)” of the Ministry of Education, Culture, Sports, Science and Technology at University of Tsukuba (JPMXP1225BA0018).

### AUTHOR INFORMATION



### Corresponding Author

Department of Applied Physics, Institute of Pure and Applied Sciences, University of Tsukuba,  
Tsukuba, Ibaraki 305-8573, Japan

\* T.S: [suemasu.takashi.gu@u.tsukuba.ac.jp](mailto:suemasu.takashi.gu@u.tsukuba.ac.jp)

### Notes

The authors declare no competing interests.



## REFERENCES

- 1) M. A. Green, E. D. Dunlop, M. Yoshita, N. Kopidakis, K. Bothe, G. Siefer, X. Hao and J. Y. Jiang, *Prog. Photovoltaics*, 2025, 33(1), 3-15.
- 2) K. Toh, T. Saito and T. Suemasu, *Jpn. J. Appl. Phys.* 2011, **50**, 068001.
- 3) M. Kumar, N. Umezawa and M. Imai, *Appl. Phys. Express* 2014, **7**, 071203.
- 4) D.B. Migas, V.L. Shaposhnikov and V.E. Borisenko, *Phys. Status Solidi B* 2007, **244**, 2611-2618.
- 5) M. Baba, K. Toh, K. Toko, N. Saito, N. Yoshizawa, K. Jiptner, T. Sekiguchi, K.O. Hara, N. Usami and T. Suemasu, *J. Cryst. Growth* 2012, 348, 75-79.
- 6) K.O. Hara, N. Usami, K. Nakamura, R. Takabe, M. Baba, K. Toko and T. Suemasu, *Appl. Phys. Express* 2013, **6**, 112302.
- 7) R. Takabe, K. O. Hara, M. Baba, W. Du, N. Shimada, K. Toko, N. Usami and T. Suemasu, *J. Appl. Phys.* 2014, **115**, 193510.
- 8) N.M. Shaalan, K.O. Hara, C.T. Trinh, Y. Nakagawa and N. Usami, *Mater. Sci. Semi. Processing*, 2018, **76**, 37.
- 9) T. Suemasu and N. Usami, *J. Phys. D: Appl. Phys.* 2017, **50**, 023001.
- 10) M. Kumar, N. Umezawa and M. Imai, *Jpn. J. Appl. Phys.* 2020, **59**, SF0803.
- 11) T. Suemasu and D. B. Migas, *Phys. Status Solidi A* 2022, **219**, 2100593
- 12) T. Sato, Y. Cao, M. Imai, J.-M. Mouesca, T. Suemasu and S. Gambarelli, *Jpn. J. Appl. Phys.* 2025, **64**, 120802.
- 13) S. Yachi, R. Takabe, H. Takeuchi, K. Toko and T. Suemasu, *Appl. Phys. Lett.* 2016, **109**, 72103.
- 14) M. Fujiwara, K. Takahashi, Y. Nakagawa, K. Gotoh, T. Itoh, Y. Kurokawa and N. Usami, *AIP Adv.* 2022, **12**, 045115.
- 15) S. Aonuki, Y. Yamashita, G. Limodio, S. Narita, K. Takayanagi, A. Iwai, K. Toko, M. Zeman, O. Isabella and T. Suemasu, *Prog. Photovolt.* 2023, **31**, 1360.
- 16) Y. Yamashita, C. M. R. Tobon, R. Santbergen, M. Zeman, O. Isabella and T. Suemasu, *Sol. Energy Mater. Sol. Cells* 2021, **230**, 111181.
- 17) K. O. Hara, K. Arimoto, J. Yamanaka and K. Nakagawa, *Jpn. J. Appl. Phys.* 2019, **58**, SBBF01.
- 18) K. Kodama, Y. Yamashita, K. Toko and T. Suemasu, *Appl. Phys. Express* **12**, 041005 (2019).
- 19) Y. Kurokawa, T. Yoshino, K. Gotoh, S. Miyamoto and N. Usami, *Jpn. J. Appl. Phys.* 2022,



61, SC1029.

20) K. Takahashi, Y. Nakagawa, K. O. Hara, Y. Kurokawa and N. Usami, *Jpn. J. Appl. Phys.* 2017, **56**, 05DB04.

21) Q. R. Deng, H. Chen, H. Liao, L. Chen, G. M. Wang, S. G. Wang and Y. L. Shen, *J. Phys. D: Appl. Phys.* 2018, **52**, 07550.

22) L. Chen, H. Chen, Q. R. Deng, G. M. Wang and S. G. Wang, *Solid State Electron.* 2018, **149**, 46.

23) M. M. A. Moon, M. H. Ali, M. F. Rahman, A. Kuddus, J. Hossain and A. M. Ismail, *Phys. Scr.* 2020, **95**, 035506.

24) K. O. Hara, *J. Phys. Chem. C* 2021, **125**, 24310.

25) H. Liao, C. A. M. Cheng, G. M. Wang, S. G. Wang, P. F. Li and Q. R. Deng, *Mod. Phys. Lett. B* 2021, **35**, 2150521.

26) K.O. Hara, *Journal of Physical Chemistry C* 2021, **125**, 24310.

27) K. O. Hara, *Sol. Energy* 2022, **245**, 136.

28) Y. Ishiguro, S. Aonuki, K. Hayashi, K. Toko and T. Suemasu, *Jpn. J. Appl. Phys.* 2025, **64**, 11SP14.

29) M.F. Rahman, M.A.B. Shanto, M.A. Ali, L. Marasamy, A. Nenami, A.R. Chaudhry, A. Irfan, *Emergent Mater.* 2025, **8**, 1395.

30) T. Yazaki, K. Arimoto, J. Yamanaka, K.O. Hara, *Science and Technology of Advanced Materials*, 2026, **6**, 2617671.

31) A. Sasaki, Y. Kataoka, K. Aoki, S. Saito, K. Kobayashi, T. Ito, K. Kakushima and H. Iwai, *Jpn. J. Appl. Phys.* 2015, **54**, 031202.

32) T. Suemasu, K. Morita, M. Kobayashi, M. Saida and M. Sasaki, *Jpn. J. Appl. Phys.* 2006, **45**, L519.

33) C. M. Wu and E. S. Yang, *Solid State Electron* 1979, **22**, 241.

34) K. Yang, J. R. East and G. I. Haddad, *Solid State Electron.* 1993, **36**, 321.

35) E. Danielsson, C. M. Zetterling, M. Ostling, D. Tsvetkov and V. A. Dmitriev, *J. Appl. Phys.* 2002, **91**, 2372.

36) S. Ahmmed, A. Aktar, M. F. Rahman, J. Hossain and A. B. M. Ismai, *Optik* 2020, **223**, 165625.

37) H. Takenaka, H. Hasebe, K. Kido, R. Koitabashi, M. Mesuda, K. Toko and T. Suemasu, *Jpn. J. Appl. Phys.* 2023, **62**, 1011.



- 38) M. Shasti and A. Mortezaali, *Phys. Status Solidi A* 2019, **216**, 1900337.
- 39) C. Messmer, M. Bivour, J. Schon, S. W. Glunz and M. Hermle, *IEEE J. Photovolt.* 2018, **8**, 456.
- 40) D. Scire, P. Procel, A. Gulino, O. Isabella, M. Zeman and I. Crupi, *Nano Res.* 2020, **13**, 3416.
- 41) M. K. Otoufi, M. Ranjbar, A. Kermanpur, N. Taghavinia, M. Minbashi, M. Forouzandeh and F. Ebadi, *Sol. Energy* 2020, **208**, 697.
- 42) J. M. Berak and M. J. Sienko, *J. Solid State Chem.* 1970, **2**, 109.
- 43) A. Paliwal, A. Sharma, M. Tomar and V. Gupta, *J. Appl. Phys.* 2014, **115**, 043104.
- 44) A. Kuddus, M. F. Rahman, S. Ahmmed, J. Hossain and A. B. M. Ismail, *Superlattices Microstruct.* 2019, **132**, 106168.
- 45) L. Cao *et al.*, *Prog. Photovolt.* 2023, **31**, 1245.
- 46) Y. Fukaya, S. Aonuki, K. Kajihara, K. Toko and T. Suemasu, *Mater. Sci. in Semi. Processing* 2025, **197**, 109732.
- 47) A. Bouhemadou, *Comput. Mater. Sci.* 2006, **38**, 263.
- 48) M. Durandurdu, *Chem. Phys.* 2010, **367**, 80.
- 49) R.J. Zollweg, *Phys. Rev.* 1958, **111**, 113.
- 50) Y. Kaneko and T. Koda, *J. Cryst. Growth* 1988, **86**, 72-78.
- 51) C.Y. Hu and E.B. Hensley, *J. Appl. Phys.* **1969**, 40, 3346.
- 52) Q. Zhao, X. Duan, T. Tian and L. Yi, *Optical Mater.* 2024, **149**, 115010.
- 53) Y. Chen, S.W. Fan and G.Y. Gao, *Phys. Chem. Chem. Phys.* 2023, **25**, 11745.
- 54) V. Saanila, J. Ihanus, M. Ritala and M. Leskela, *Chem. Vap. Deposition* 1998, **4**, 227.
- 55) T. Sato, Islam Md. Ariful, K. Hayashi, Y. Fukaya, R. Du, M. Hirai, Y. Koda, M. Mesuda, K. Toko and T. Suemasu, *Jpn. J. Appl. Phys.* 2025, **64**, 12SP13.
- 56) H. Hasebe, K. Kido, H. Takenaka, M. Mesuda, K. Toko and T. Suemasu, *Jpn. J. Appl. Phys.* 2023, **62**, SD1010.
- 57) R. Takabe, H. Takeuchi, W. Du, K. Ito, K. Toko, S. Ueda, A. Kimura and T. Suemasu, *J. Appl. Phys.* 2016, **119**, 165304.
- 58) G. Kresse and J. Hafner, *Phys. Rev. B* 1994, **49**, 14251.
- 59) G. Kresse and J. Furthmü, *Phys. Rev. B* 1996, **54**, 11169.
- 60) G. Kresse and D. Joubert, *Phys. Rev. B* 1999, **59**, 1758.
- 61) J. P. Perdew, K. Burke and M. Ernzerhof, *Phys. Rev. Lett.* 1996, **77**, 3865.



- 62) H. J. Monkhorst and J. D. Pack, *Phys. Rev. B* 1976, **13**, 5188.
- 63) S. Kim, S. N. Hood, J. S. Park, L. D. Whalley and A. Walsh, *J. Phys. Energy* 2020, **2**, 036001.
- 64) F. A. Kröger and H. J. Vink, *Solid State Physics* 1956, **3**, 307-435.
- 65) C.G. Van de Walle, *J. Appl. Phys.* 2004, **95**, 3851.
- 66) S. Lany and A. Zunger, *Phys. Rev. B* 2008, **78**, 235104.
- 67) I. Borukhov, D. Andelman and H. Orland, *Phys. Rev. Lett.* 1997, **79**, 435-438.
- 68) K. Momma and F. Izumi, *J. Appl. Crystallogr.* 2011, **44**, 1272.
- 69) M. Imai and T. Hirano, *Phys. Rev. B* 1998, **58**, 11922.
- 70) S. Badyakar, G.M. Rao and C. Das, *Discov. Electron* 2026, **3**, 87.
- 71) G. E. Jellison and F. A. Modine, *Appl. Phys. Lett.* 1996, **69** (3), 371.
- 72) Erratum, G. E. Jellison and F. A. Modine, *Appl. Phys. Lett.* 1996, **69** (14), 2137.
- 73) H. Chen and W. Z. Shen, *Eur. Phys. J. B.* 2005, **43**, 503.
- 74) M. Zhong, W. Zeng, F.S. Liu, D.H. Fan, B. Tang and Q.J. Liu, *Mater. Today Phys.* 2022, **22**, 100583.
- 75) V. Ha, G. Yu, F. Ricci, D. Dahliah, M.J. van Setten, M. Giantomassi, G. Rignanese and G. Hautier, *Phys. Rev. Mater.* 2019, **3**, 034601.
- 76) M. Dadsetani and A. Pourghazi, *Optics Commun.* 2006, **266**, 562.
- 77) S. Drablia, H. Meradji, S. Ghemid, G. Nouet and E. El Haj Hassan, *Comput. Mater. Sci.* 2009, **46**, 376.
- 78) B. Aminour, M. Slimani, G. Sifi, R. Khemissi, H. Meradji, G. Sebti, S. Binomran and R. Khenata, *Chin. J. Phys.* 2017, **55**, 367.
- 79) M. Kumar, N. Umezawa, W. Zhou and M. Imai, *J. Mater. Chem. A* 2017, **5**, 25293.
- 80) Y. Imai, M. Sohma and T. Suemasu, *Jpn. J. Appl. Phys.* 2015, **54**, 07JE03.



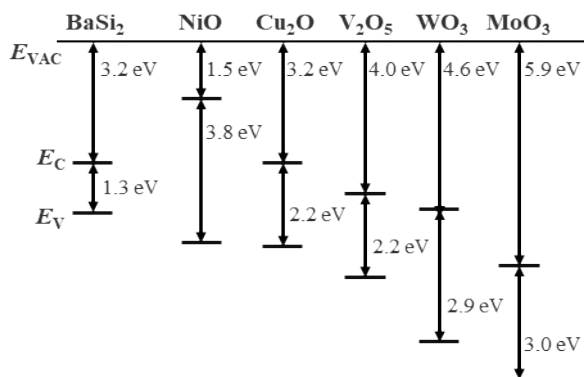


Fig. 1. Band alignment of BaSi<sub>2</sub> and HTL candidate materials<sup>33-41</sup> with respect to the vacuum level  $E_{VAC}$ .



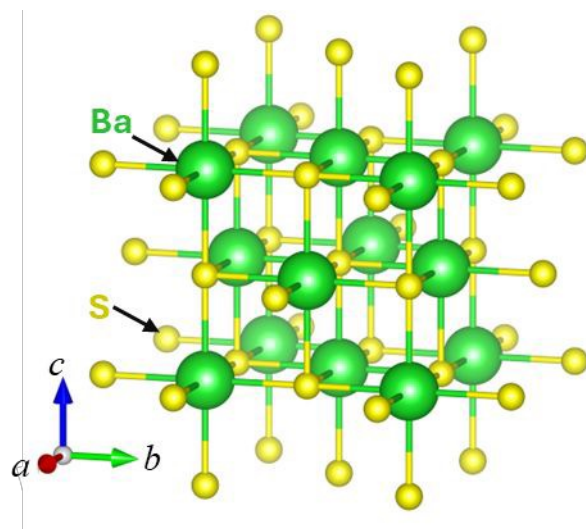


Fig. 2. Unit cell of BaS with space group of  $Fm\bar{3}m$ . Green and yellow spheres represent Ba and S, respectively.



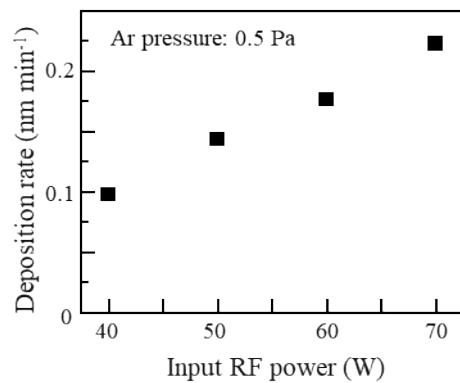


Fig. 3. Dependence of deposition rate of BaS films on input RF power to the BaS target obtained in this work.



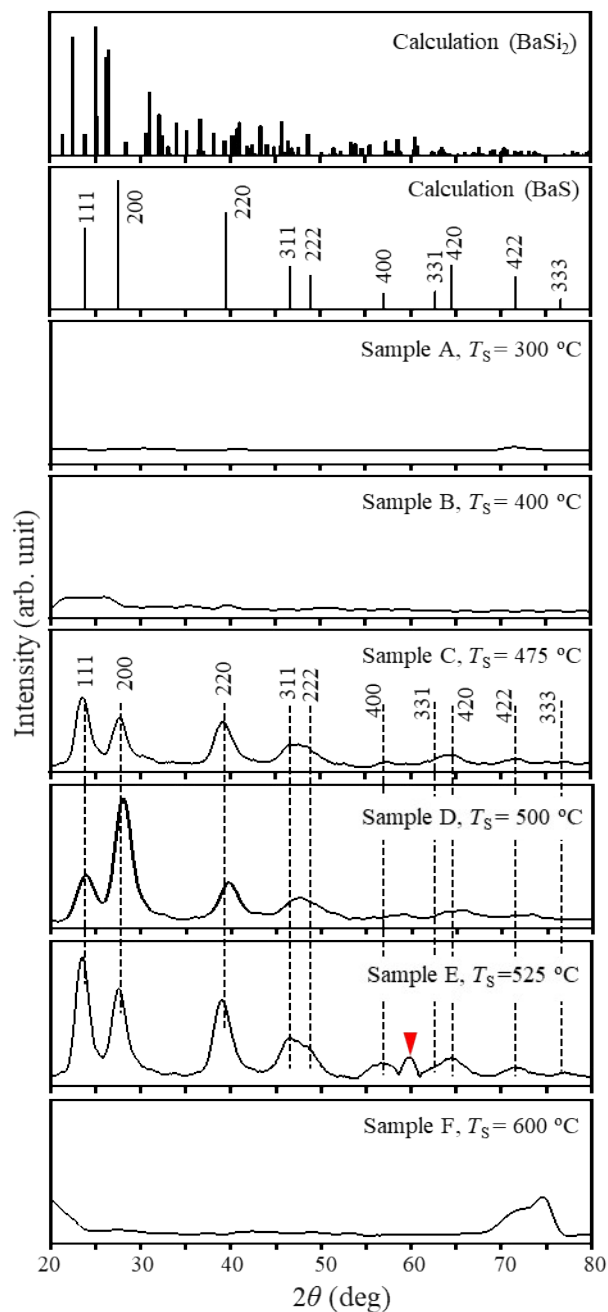


Fig. 4. GI-XRD patterns of samples A-F, prepared at different substrate temperatures. Calculation results for  $\text{BaSi}_2$  and  $\text{BaS}$  are also shown. Red triangle shows the peak position corresponding to  $\text{BaSi}_2$ . The discontinued lines are guide to the eye.



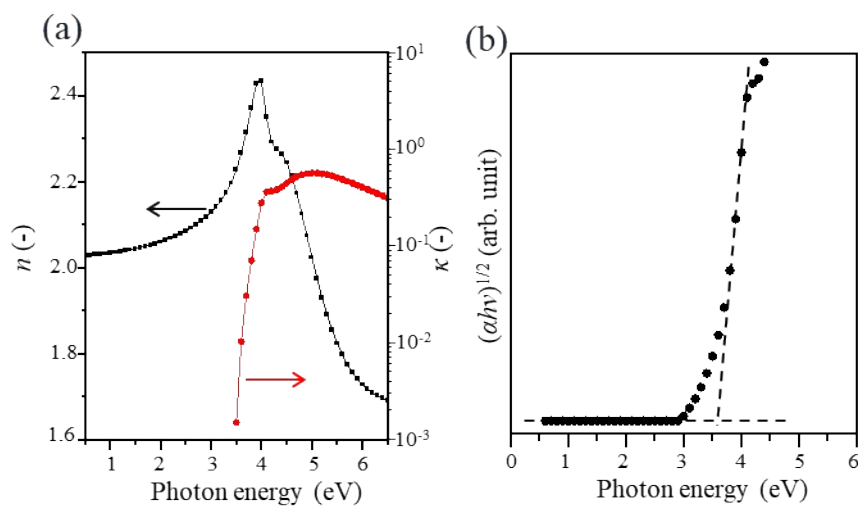


Fig. 5 (a) Measured data points of refractive index  $n$  and extinction coefficient ( $\kappa$ ) obtained for sample G. (b)  $(\alpha h\nu)^{1/2}$  plot against photon energy. The broken line is guide to the eye.



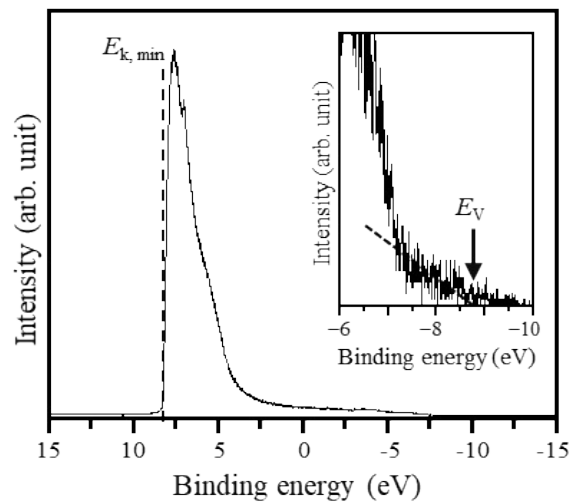


Fig. 6. UPS spectrum of the BaS film in sample D. Enlarged view around  $E_V$  is inserted.



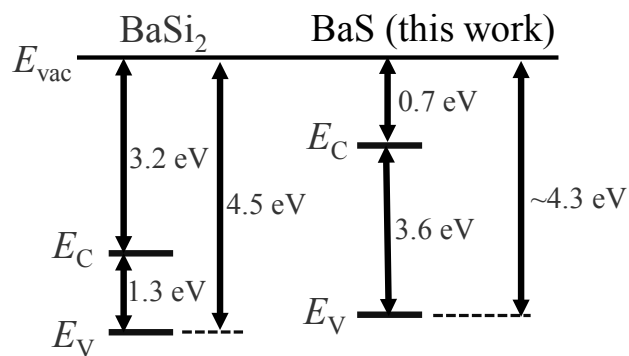


Fig. 7. Band alignment of BaSi<sub>2</sub><sup>2,31,32</sup> and BaS.



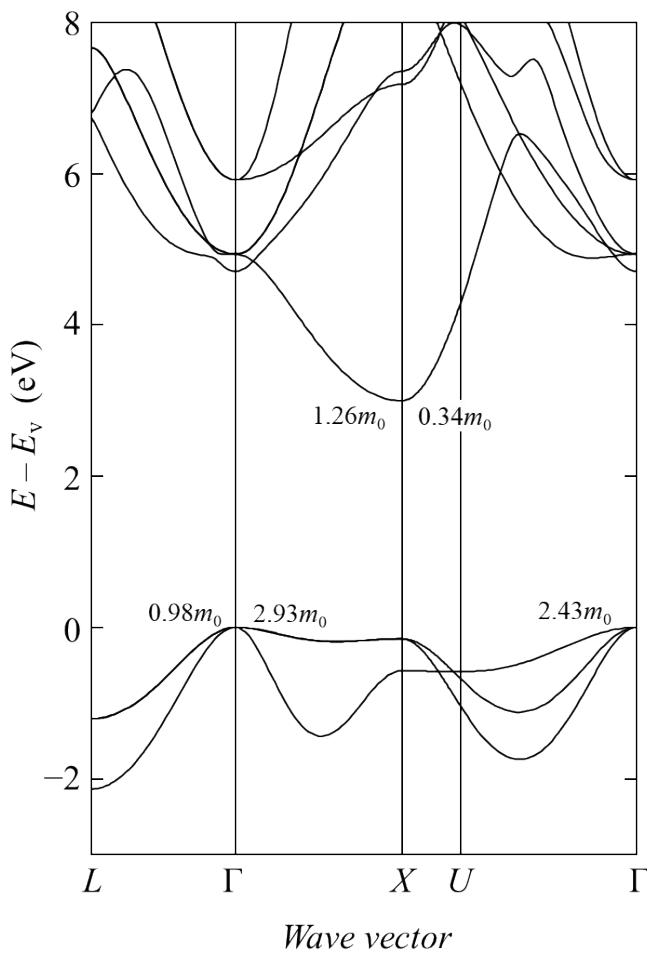


Fig. 8. Energy band structure of BaS calculated using the HSE functional. Effective masses of electrons and holes are also shown using the mass of a free electron  $m_0$ .



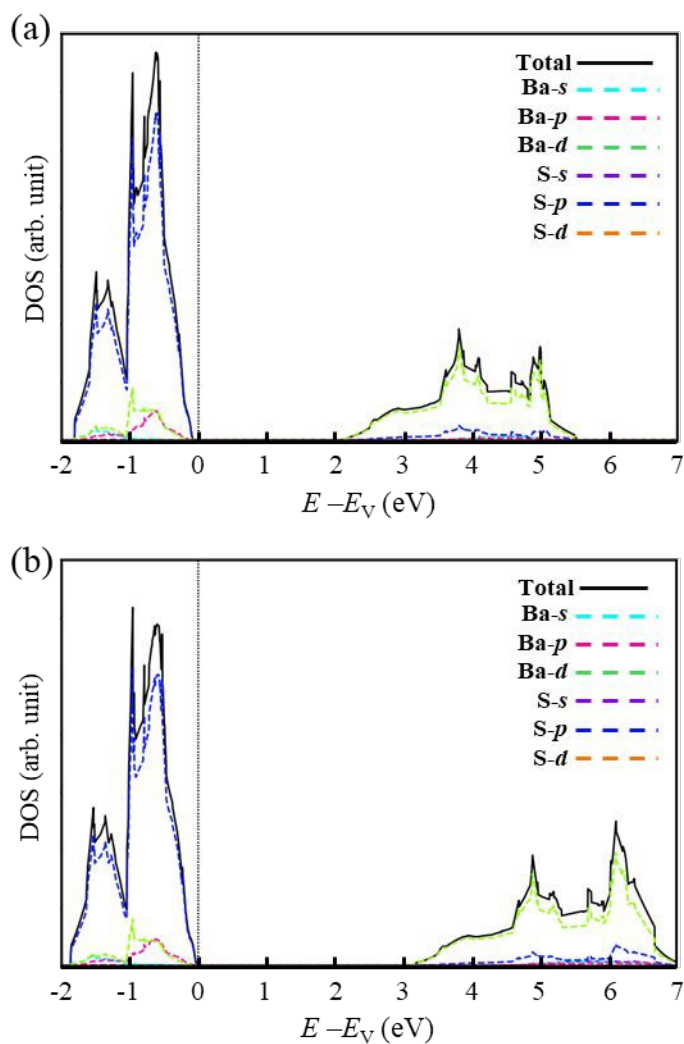


Fig. 9. Projected DOS of BaS calculated using (a) the GGA functional and (b) the HSE functional, with energies referenced to  $E_V$ .



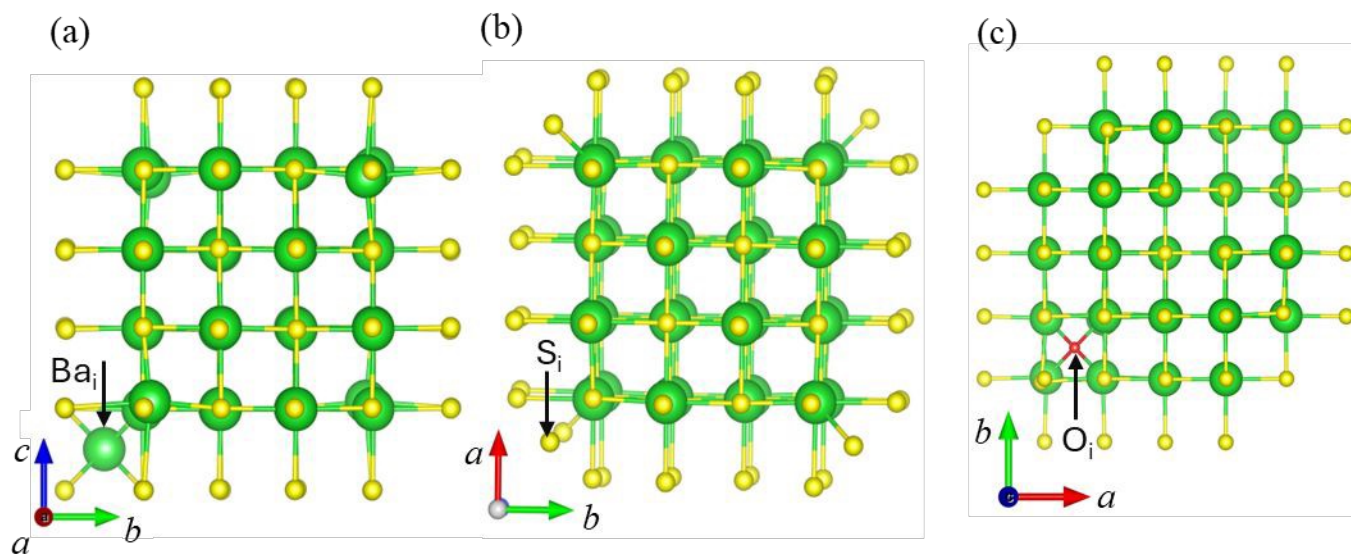


Fig. 10. Relaxed atomic structures of interstitial defects in BaS: (a)  $Ba_i$ , (b)  $S_i$ , and (c)  $O_i$  initially introduced at the interstitial site with fractional coordinates (0.125, 0.125, 0.125) and fully relaxed the local geometry. Arrows indicate the interstitial atoms. Green, yellow, and red spheres represent Ba, S, and O, respectively.



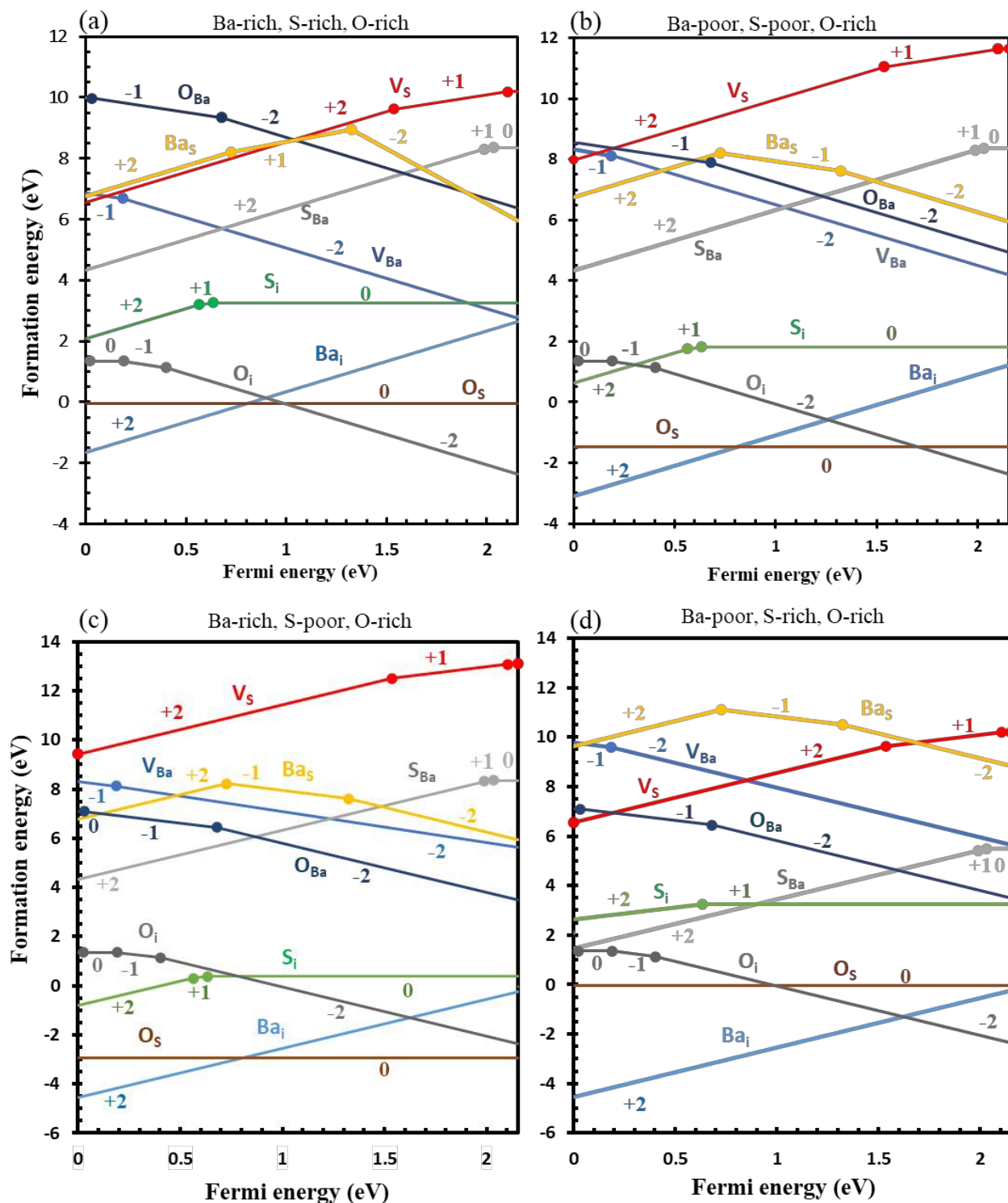


Fig. 11. Calculated formation energies against Fermi energy in BaS under (a) Ba-rich, S-rich, O-rich, (b) Ba-poor, S-poor, O-rich, (c) Ba-rich, S-poor, O-rich, and (d) Ba-poor, S-rich, O-rich conditions.



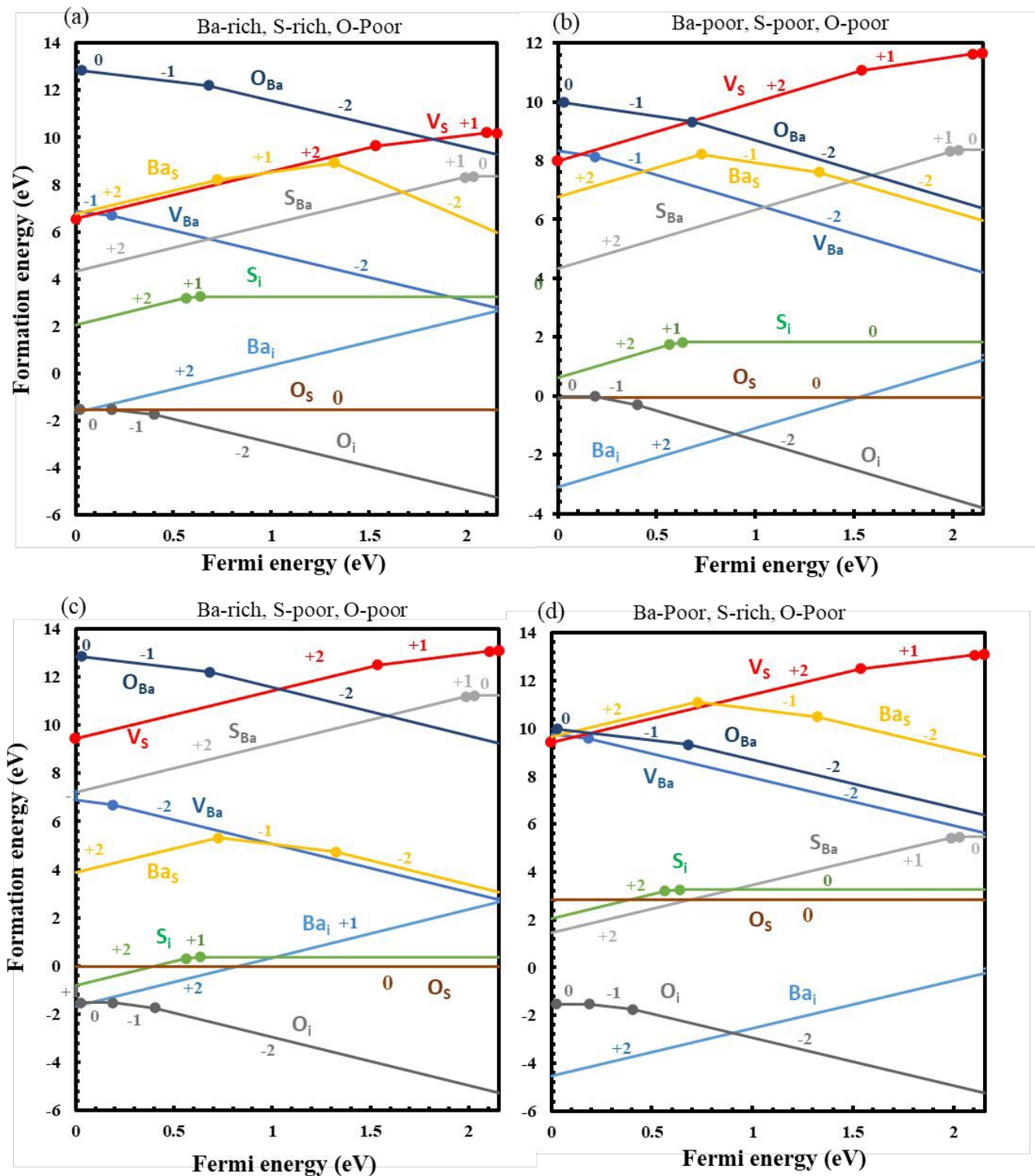


Fig. 12. Calculated formation energies against Fermi energy in BaS under (a) Ba-rich, S-rich, O-poor, (b) Ba-poor, S-poor, O-poor, (c) Ba-rich, S-poor, O-poor, and (d) Ba-poor, S-rich, O-poor conditions.



The data that support the findings of this study are available from the corresponding author upon reasonable request.

